Radiation Dosimetry of the Fibrin-Binding Probe ^{64}Cu-FBP8 and Its Feasibility for PET Imaging of Deep Vein Thrombosis and Pulmonary Embolism in Rats

Francesco Blasi[1], Bruno L. Oliveira[1], Tyson A. Rietz[1], Nicholas J. Rotile[1], Helen Day[1], Pratap C. Naha[2], David P. Cormode[2], David Izquierdo-Garcia[1], Ciprian Catana[1], and Peter Caravan[1,3]

[1]Department of Radiology, Athinoula A. Martinos Center for Biomedical Imaging, Massachusetts General Hospital, Harvard Medical School, Charlestown, Massachusetts; [2]Department of Radiology, Perelman School of Medicine, University of Pennsylvania, Philadelphia, Pennsylvania; and [3]Institute for Innovation in Imaging, Massachusetts General Hospital, Boston, Massachusetts

The diagnosis of deep venous thromboembolic disease is still challenging despite the progress of current thrombus imaging modalities and new diagnostic algorithms. We recently reported the high target uptake and thrombus imaging efficacy of the novel fibrin-specific PET probe ^{64}Cu-FBP8. Here, we tested the feasibility of ^{64}Cu-FBP8 PET to detect source thrombi and culprit emboli after deep vein thrombosis and pulmonary embolism (DVT-PE). To support clinical translation of ^{64}Cu-FBP8, we performed a human dosimetry estimation using time-dependent biodistribution in rats. **Methods:** Sprague–Dawley rats ($n = 7$) underwent ferric chloride application on the femoral vein to trigger thrombosis. Pulmonary embolism was induced 30 min or 2 d after DVT by intrajugular injection of a preformed blood clot labeled with ^{125}I-fibrinogen. PET imaging was performed to detect the clots, and SPECT was used to confirm in vivo the location of the pulmonary emboli. Ex vivo γ counting and histopathology were used to validate the imaging findings. Detailed biodistribution was performed in healthy rats ($n = 30$) at different time points after ^{64}Cu-FBP8 administration to estimate human radiation dosimetry. Longitudinal whole-body PET/MR imaging ($n = 2$) was performed after ^{64}Cu-FBP8 administration to further assess radioactivity clearance. **Results:** ^{64}Cu-FBP8 PET imaging detected the location of lung emboli and venous thrombi after DVT-PE, revealing significant differences in uptake between target and background tissues ($P < 0.001$). In vivo SPECT imaging and ex vivo γ counting confirmed the location of the lung emboli. PET quantification of the venous thrombi revealed that probe uptake was greater in younger clots than in older ones, a result confirmed by ex vivo analyses ($P < 0.001$). Histopathology revealed an age-dependent reduction of thrombus fibrin content ($P = 0.006$), further supporting the imaging findings. Biodistribution and whole-body PET/MR imaging showed a rapid, primarily renal, body clearance of ^{64}Cu-FBP8. The effective dose was 0.021 mSv/MBq for males and 0.027 mSv/MBq for females, supporting the feasibility of using ^{64}Cu-FBP8 in human trials. **Conclusion:** We showed that ^{64}Cu-FBP8 PET is a feasible approach to image DVT-PE and that radiogenic adverse health effects should not limit the clinical translation of ^{64}Cu-FBP8.

Key Words: thrombosis; PET imaging; fibrin; DVT-PE; dosimetry

J Nucl Med 2015; 56:1088–1093
DOI: 10.2967/jnumed.115.157982

Despite recent advances, limitations remain in the tests used to diagnose acute pulmonary embolism (PE) and deep vein thrombosis (DVT). Although contrast-enhanced CT has become the gold standard for PE (*1,2*), its sensitivity decreases as the location of the PE becomes more distal (*3*). Furthermore, contrast-enhanced CT is contraindicated in patients with poor renal function because of the risk of contrast-induced nephrotoxicity. Ventilation–perfusion lung scanning has a specificity comparable to thoracic CT (*4,5*), but its sensitivity is lower (*4*), and there are often uninterpretable scans. Diagnosis of DVT involves clinical prediction guide, D-dimer, and venous ultrasound, but again there are limitations. Up to 10% of patients with a moderate-to-high clinical suspicion for DVT will have DVT despite a normal venous ultrasound (*6*). Ultrasound may not distinguish old from new disease when there is suspicion of recurrent DVT (*7*). Finally, ultrasound is technically difficult in obese or edematous patients, is not possible for imaging the pelvic veins, and is not possible in the presence of orthopedic casts and other immobilization devices. Venography or contrast-enhanced CT may be used, but these are avoided in patients with renal insufficiency (*8*). Furthermore, neither ultrasound nor CT is informative about the composition of the thrombus and the fibrin content, although therapeutic strategies (e.g., thrombolysis vs. thrombectomy) may benefit from such information (*9*).

Direct targeting of the thrombus components using molecular imaging offers instead a noninvasive solution with high sensitivity and specificity as well as potential whole-body applications (*10*). In particular, fibrin is an ideal target for molecular imaging of thrombosis because it is present at high concentrations in both venous and arterial clots but not in circulating blood, resulting in potential high sensitivity and specificity of detection (*11*). We recently screened a series of fibrin-binding PET probes (*12–16*). These probes were based on short 6-aminoacid cyclic peptides that displayed submicromolar affinity for fibrin and high selectivity (>100-fold) for fibrin over fibrinogen or plasma proteins (*17,18*). The probe ^{64}Cu-FBP8 emerged as the best candidate for further testing because of its high affinity for fibrin, fast blood clearance, and high metabolic stability (*16*).

Received Mar. 22, 2015; revision accepted Apr. 27, 2015.
For correspondence or reprints contact: Peter Caravan, Bldg. 149, Rm. 2301, 13th St., Charlestown, MA 02129.
E-mail: caravan@nmr.mgh.harvard.edu
Published online May 14, 2015.

In the present study, we aimed to assess the feasibility of ^{64}Cu-FBP8 PET as a single thrombus imaging approach to detect source thrombi and culprit emboli in a model of venous thromboembolism. Furthermore, we performed time-dependent biodistribution to estimate the human dosimetry of ^{64}Cu-FBP8 to support its bench-to-bedside translation.

MATERIALS AND METHODS

^{64}Cu-FBP8

^{64}Cu-FBP8 was synthesized in quantitative yield (purity > 99% by high-performance liquid chromatography) as previously reported (*16*), with a specific activity of 6–12 GBq/μmol. ^{64}Cu-FBP8 comprises a cyclic disulfide peptide FHCHypY(3-Cl)DLCHIL-PXD (Hyp = *L*-4-hydroxyproline; Y(3-Cl) = *L*-3-chlorotyrosine; PXD = *para*-xylenediamine) conjugated to the chelator NODAGA (1,4,7-triazacyclononane,1-glutaric acid-4,7-acetic acid) at the C and N termini and labeled with ^{64}Cu (Supplemental Fig. 1; supplemental materials are available at http://jnm.snmjournals.org). ^{64}Cu-FBP8 has high affinity for the soluble fibrin fragment DD(E) (K_i = 430 nM), is stable in blood after intravenous administration (>90% intact probe up to 4 h after injection), and clears predominantly by the renal pathway (plasma half-life, 14 min) (*16*).

Animal Model of DVT and PE

Animal experiments were performed in accordance with the National Institutes of Health *Guide for the Care and Use of Laboratory Animals* (*19*) and were approved by the Institutional Animal Care and Use Committee at Massachusetts General Hospital. Adult male Sprague–Dawley rats (n = 7, 250–300 g; Charles River Laboratories) were anesthetized with isoflurane (4% induction, 2%–2.5% maintenance, in medical air) and placed supine on a homeothermic blanket. PE was induced by injection of a preformed blood clot in the pulmonary circulation from the external jugular vein (*20*). To identify the location of pulmonary emboli, clots were prepared by mixing 200 μL of freshly withdrawn arterial blood with ^{125}I-fibrinogen (50 μL, 2 MBq), which was converted to ^{125}I-fibrin and incorporated into the thrombus (*20*). The mixture was allowed to clot in a PE-90 tube for 2 h at room temperature and then overnight at 4°C. The resulting ^{125}I emboli were rinsed in saline and then stained with Evans blue dye (2% w/v, in sterile saline; Sigma) before injection to enhance postmortem visualization. Femoral vein thrombosis was induced in all animals by ferric chloride application either 30 min or 2 d before pulmonary embolism to mimic a DVT-PE scenario. DVT was induced using the ferric chloride model (*21*). A small piece of filter paper was soaked for 1 min in a solution of ferric chloride (25% w/v, in sterile saline; Sigma) and then applied on the femoral vein for 5 min. At the end of the procedure, the surgical site was rinsed with sterile saline to remove the excess of ferric chloride, and the formation of the clot was confirmed by visual inspection.

Probe Administration and Imaging Protocol

Rats were positioned prone in a small-animal PET/SPECT/CT scanner (Triumph; TriFoil Imaging) equipped with respiratory monitoring, heating pad system, and inhalation anesthesia (isoflurane, 2%–2.5%). Instrument calibration was performed with phantoms containing small known amounts of radioactivity. Each rat was injected via the tail vein with 10 MBq in a volume of 300 μL, followed by saline flush. The injected dose was calculated by the difference of the radioactivity in the syringe before and after the administration, as measured by a dose calibrator (CRC-25PET; Capintec) (*14–16*). The hindlimbs (isocenter: femoral vein) were imaged first for 30 min starting 45 min after probe administration, followed by a 90-min acquisition of the chest (isocenter: lungs) to detect the pulmonary embolus. SPECT (energy peak, 35.5 keV ± 15%; 4 detector head mounting collimators equipped with 5 circular 2.5-mm pinholes; 90° rotation, 16 projections, 38 s per projection) was performed to image the ^{125}I emboli. At the end of each PET imaging session, a CT scan was obtained over 4.27 min with 512 projections and 2 frames per projection (peak tube voltage, 70 kV; tube current, 177 mA). A polyethylene glycol–coated gold nanoparticle contrast agent (300 mg/kg, intravenous) was injected before the CT scan for angiography. Gold nanoparticle cores were synthesized by reduction of gold chloride with sodium citrate in boiling water (Turkevich method). The cores were subsequently capped with thiol-PEG-2000, purified via washing with phosphate-buffered saline followed by centrifugation, concentrated to about 75 mg/mL, and sterilized via filtration before use (*22*).

PET, SPECT, and CT images were reconstructed using the LabPET and the X-SPECT software (TriFoil Imaging) to a voxel size of 0.5 × 0.5 × 0.6 mm (PET), 1.3 × 1.3 × 0.9 mm (SPECT), and isotropic 0.3 mm^3 (CT). All images were corrected for decay, randoms, and dead time, and the CT data were used to provide attenuation correction. The PET data were reconstructed using a maximum-likelihood expectation maximization algorithm run over 30 iterations, whereas for SPECT data an ordered-subset expectation maximization algorithm run over 5 iterations and 4 subsets was used. Reconstructed data were quantitatively evaluated using AMIDE (*23*), by drawing volumes of interest on the pulmonary or cardiac embolus (4.2 mm^3) and adjacent nonthrombosed lung and cardiac tissue (4.2 mm^3), thrombosed and contralateral veins (4.2 mm^3), muscle (calf, 65.4 mm^3), and bone (sternum and tibia, 4.2 mm^3). Because the location of the pulmonary embolus was different in each animal, volumes of interest were directly drawn on fused PET/CT images. For the femoral thrombi, volumes of interest were first placed on the vein using CT-only images and then centered on the hot spot using fused PET/CT images. PET data are expressed as percentage injected activity (dose) per cubic centimeter.

Ex Vivo Studies

Animals were euthanized at the end of the imaging experiments and tissues harvested and processed for ex vivo analyses. The radioactivity of the thrombosed and contralateral femoral veins, lung, heart, muscle, and bone was quantified with a γ counter (Wizard^2; PerkinElmer) to determine the percentage injected activity (dose) per gram of tissue (*14–16*). To further confirm the location of the ^{125}I emboli in PE studies, samples were recounted after ^{64}Cu was fully decayed. Histopathology was performed to evaluate thrombus morphology and composition. Fresh-frozen, formalin-fixed vessels were cryosectioned (20-μm thickness, 500-μm interval) to sample the entire length of the thrombus and then stained using the trichrome method Martius scarlet blue (MSB), which allows differentiation between erythrocytes (yellow), fibrin (purple-red), and collagen (blue) (*24*). Color segmentation was performed using ImageJ software (National Institutes of Health); the total fibrin volume for each thrombus was obtained by integrating the sum of the areas occupied by the fibrin with the interval between adjacent sections (*25–27*). This method shows high correlation with fibrin quantification obtained with Western blot analysis (*25–27*). To confirm the specificity of our staining in detecting fibrin, adjacent histologic slices were stained with hematoxylin and eosin, MSB, and an antifibrin α-chain antibody (U45, 10 μg/mL; Abcam), as previously reported (*15*). Negative control experiments were performed by omitting the primary antibody. Images were acquired using a microscope equipped with epifluorescence illumination (TE-2000; Nikon).

Human Dosimetry Estimation from Animal Biodistribution and Whole-Body PET/MR Imaging

Biodistribution of ^{64}Cu-FBP8 in healthy rats was performed after intravenous administration of the probe (n = 30). Animals were euthanized at 5 min, 30 min, 3 h, 6 h, and 24 h after injection (3 males and 3 females per time point), and the following tissues and organs were collected: blood, lungs, liver, spleen, kidneys, bladder (empty), muscle (left rectus femoris), fat, heart (empty), brain, bone (left femur), adrenals, stomach

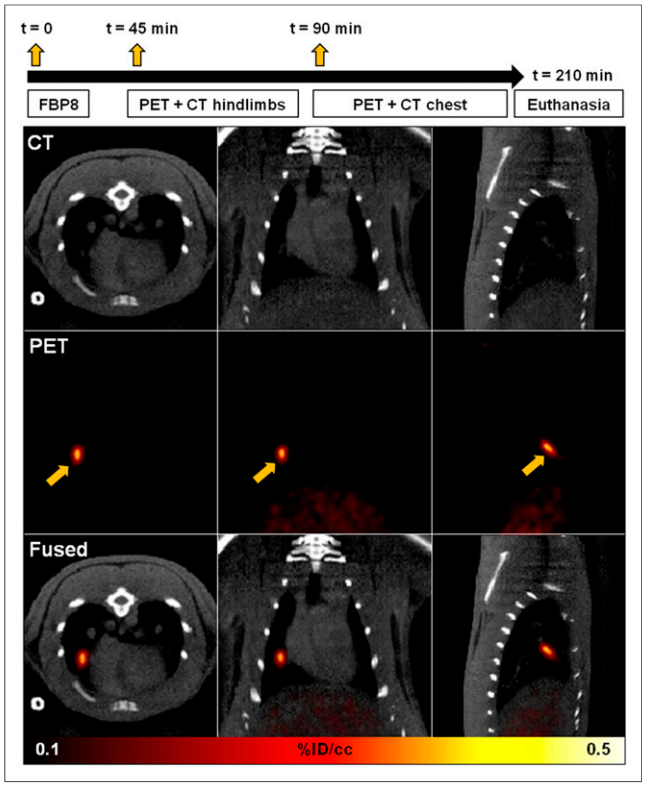

FIGURE 1. ^{64}Cu-FBP8 PET imaging of pulmonary embolism. Experimental scheme and imaging time points are shown at top. CT, PET, and fused images from representative animal injected with ^{64}Cu-FBP8 after induction of PE showing embolus detection in right middle lobe (arrows).

(empty), small intestine (empty), urine, uterus, and ovaries. The radioactivity in each tissue was measured to obtain time–activity curves and expressed as percentage injected activity (dose) per organ. Total blood volume and total mass for bone, muscle, and fat were estimated according to previously published methods (*28,29*). Animal data were extrapolated to obtain dose estimates for humans using the percentage kg/g method (*30*). The human dosimetry estimation was performed using the OLINDA/EXM (version 1.0; Vanderbilt University, 2003) software to provide quantitative information on the amount of ^{64}Cu radioactivity that accumulates in tissues and organs (*31*). A small cohort of healthy rats (n = 2, 1 male and 1 female) was imaged in a clinical PET/MR scanner, as previously reported (*12,13*). Rats were imaged for 60 min starting 2 and 24 h after ^{64}Cu-FBP8 injection. Additional information is reported in the supplemental data.

Statistics

Data are shown as box-and-whisker plots (whiskers, full range; box, 25%–75%; line, median; cross, mean). Differences between groups were analyzed using the unpaired 2-tailed t test and 1-way ANOVA followed by Tukey post hoc test. The Pearson correlation coefficient was computed to assess the quality of linear correlations, and a t statistic was calculated on the basis of the null hypothesis that the correlation coefficient was zero. A P value of less than 0.05 was considered significant.

RESULTS

Detection of DVT-PE with ^{64}Cu-FBP8 PET

Rats, with a femoral vein thrombus and an embolus to either the lungs or the heart chambers, were imaged according to the scheme depicted in Figure 1. ^{64}Cu-FBP8 PET identified emboli in the lungs (6 rats) and cardiac chambers (1 rat) after thromboembolism via the jugular vein, with the pulmonary embolus mainly affecting the right middle and inferior lobes (Supplemental Video 1). Emboli were prelabeled with ^{125}I-fibrinogen, and SPECT imaging confirmed in vivo that the location of the clots detected with ^{64}Cu-FBP8 PET corresponded to the ^{125}I emboli (Fig. 2). PET quantification showed significant differences in probe uptake between the emboli and the nearby background tissues. The presence and the location of the emboli were further confirmed after dissection of individual lung lobes and heart and by γ counting of the ^{125}I radioactivity. ^{64}Cu-FBP8 PET allowed the localization of femoral vein thrombi in the same animals with PE (Fig. 3). One rat underwent bilateral DVT 2 d and 30 min before PE to show fibrin uptake in the same subject bearing 2 thrombi of different age. PET quantification showed significant differences in target uptake between younger and older thrombi and between clots and background tissues. After euthanasia, the presence of the thrombi was confirmed in every animal by inspection of the vessels. Biodistribution analysis confirmed that the probe uptake of the fresher thrombi was higher than the uptake of the older clots. Pearson analysis showed a positive correlation between the probe uptake detected with PET quantification and γ counting. Detailed histopathology confirmed the presence of fibrin-rich venous thrombi in every animal (Fig. 4). MSB staining and volumetric quantification based on color segmentation revealed greater fibrin content in the hyperacute thrombi than in the subacute clots.

Human Dosimetry Estimation for ^{64}Cu-FBP8 from Animal Biodistribution

Detailed biodistribution revealed rapid clearance of the probe from the blood compartment as well as from muscle tissue, heart,

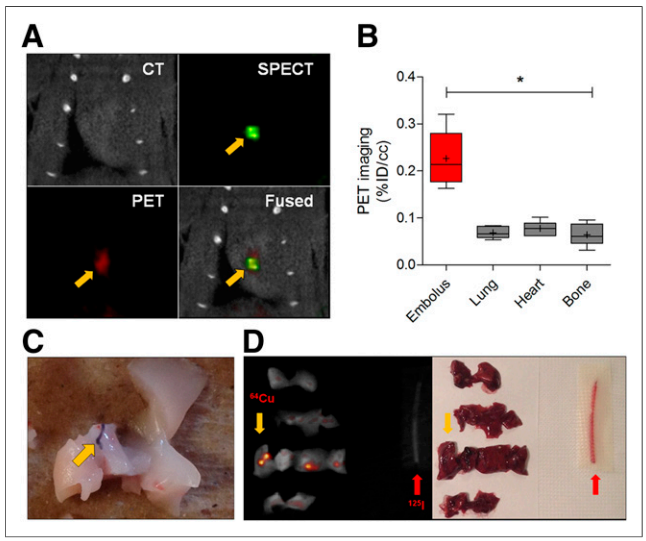

FIGURE 2. Multimodal imaging of thromboembolism. Representative multimodal PET/SPECT/CT images showing embolus detected in cardiac chamber (A, arrows) and colocalization of hyperintense region in SPECT image (^{125}I embolus, arrow) and hot spot detected with ^{64}Cu-FBP8 PET (90 min after injection). (B) PET quantification reveals significant differences in uptake between target embolus, located either in lungs or in heart and adjacent background tissues. (C) Representative images of lung lobe harvested after PE revealing presence of embolus. One rat was transcardially perfused with saline to enhance postmortem visualization of Evans blue–labeled embolus (arrow). (D) Ex vivo imaging performed on dissected lung lobes confirms presence of hot spots consistent with ^{64}Cu-FBP8 PET uptake (yellow arrow). ^{125}I embolus (red arrow) was imaged along with lung samples to confirm absence of activity spillover between SPECT and PET. *$P < 0.001$, 1-way ANOVA followed by Tukey post hoc test. n = 7.

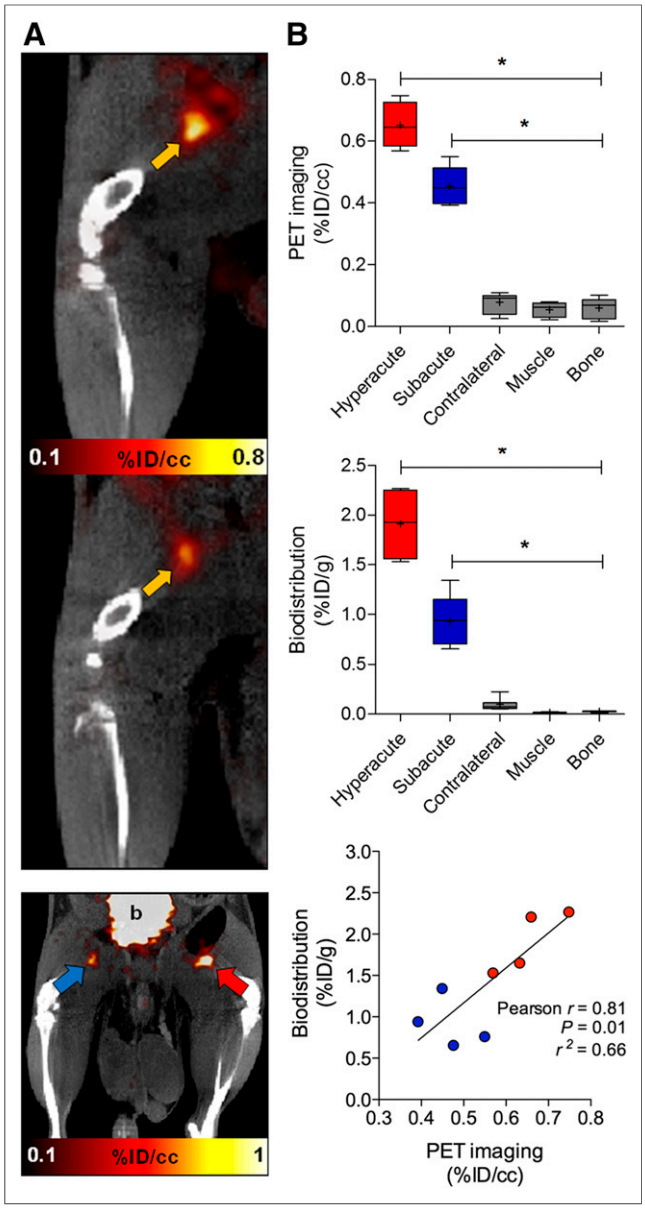

FIGURE 3. ^{64}Cu-FBP8 PET imaging of DVT. (A) Representative PET/CT images of hyperacute (~1 h old) and subacute (48 h old) femoral vein thrombi detected 45 min after probe administration. Target uptake of hyperacute (red arrow) and subacute (blue arrow) clots shown in same animal (bottom). Activity in bladder (b) is off scale. (B) Significant differences in target uptake between younger (hyperacute, $n = 4$) and older (subacute, $n = 4$) thrombi and between clots and background tissues and positive correlation between thrombus uptake assessed with PET imaging and γ counting. *$P < 0.001$, 1-way ANOVA followed by Tukey post hoc test. $n = 7$.

and lungs (Table 1). No relevant uptake was detected in the digestive tract, adrenals, spleen, bone, fat, and reproductive organs. Kidneys showed the highest uptake and retention, confirming the primary renal elimination of ^{64}Cu-FBP8 (*16*). Activity levels in the bladder wall peaked at 30 min after probe administration and then rapidly decreased, consistent with the fast urinary excretion of the probe. Notably, the liver, a target organ for unchelated ^{64}Cu, showed low radioactivity retention. Longitudinal whole-body PET/MR imaging confirmed the overall low retention of ^{64}Cu-FBP8 in all body regions and prevalent renal elimination (Fig. 5). One day after probe administration, low kidney retention was mainly localized in the renal cortex. Complete human dosimetry estimates are reported in Supplemental Table 1. Kidneys appeared as the primary critical organs, followed by the urinary bladder and liver (Table 2). We estimated the effective dose for humans to be 0.021 mSv/MBq for males and 0.027 mSv/MBq for females.

DISCUSSION

The aim of this study was to test the feasibility of ^{64}Cu-FBP8 PET as a thrombus imaging approach to detect both source thrombi and culprit emboli after DVT-PE and to provide human dosimetry estimates to support the clinical translation of ^{64}Cu-FBP8. We recently showed that ^{64}Cu-FBP8 has high target uptake, rapid systemic clearance, and low off-target retention in a model of mural carotid artery thrombosis (*16*). Here, we extended these results showing that ^{64}Cu-FBP8 PET is suitable for imaging thrombi and emboli in different vascular territories and anatomic locations including veins, pulmonary arteries, and cardiac chambers. Pulmonary emboli and deep vein thrombi were clearly detected after probe injection, suggesting that ^{64}Cu-FBP8 PET may facilitate the evaluation of thromboembolic phenomena using a whole-body, molecular imaging approach.

Molecular SPECT imaging of pulmonary emboli with the ^{99m}Tc-labeled anti–D-dimer antibody DI-80B3 has recently shown good accuracy and safety in preclinical studies and a small phase 2 human trial (*32,33*). Although the clinical performance of ^{64}Cu-FBP8 PET remains to be demonstrated, the high thrombus uptake observed in this study for both PE and DVT suggests the potential of this molecular imaging approach using PET. The high target-to-background contrast may allow imaging of emboli in the distal branches of the pulmonary circulation, detected with lower sensitivity by CT angiography (*3*). Moreover, ^{64}Cu-FBP8 PET may provide an alternative

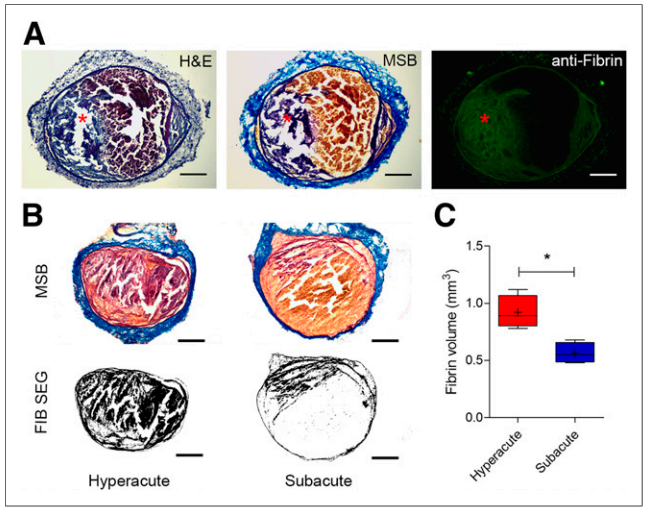

FIGURE 4. Histopathology of venous thrombi. (A) Adjacent histologic sections obtained from venous thrombus and stained with hematoxylin and eosin (H&E), MSB, and antifibrin antibody showed congruent localization of fibrin (asterisk), confirming selectivity of MSB staining for fibrin. (B) Representative coronal sections of venous thrombi stained with MSB showing age-dependent changes in thrombus composition. Color segmentation analysis for fibrin (FIB SEG) performed on MSB-stained sections showing fibrin detection. (C) Volumetric quantification of thrombus composition revealed age-dependent reduction of fibrin content. Scale bars are 0.2 mm. *$P = 0.006$, unpaired 2-tailed t test. $n = 4$/group.

TABLE 1
Biodistribution of ^{64}Cu-FBP8 in Healthy Rats

Organ	5 min	30 min	3 h	6 h	24 h
Liver	7.385 ± 0.838	5.820 ± 0.479	1.175 ± 0.276	1.390 ± 0.079	0.259 ± 0.032
Kidneys	19.787 ± 1.694	20.520 ± 6.655	14.908 ± 3.386	11.663 ± 1.466	2.946 ± 0.796
Lungs	0.961 ± 0.159	0.471 ± 0.075	0.038 ± 0.007	0.053 ± 0.008	0.009 ± 0.001
Spleen	0.261 ± 0.046	0.192 ± 0.040	0.019 ± 0.002	0.028 ± 0.008	0.006 ± 0.001
Bladder	0.078 ± 0.030	0.193 ± 0.087	0.010 ± 0.005	0.005 ± 0.001	0.0008 ± 0.0002
Heart	0.321 ± 0.026	0.159 ± 0.023	0.013 ± 0.002	0.018 ± 0.003	0.006 ± 0.001
Brain	0.055 ± 0.012	0.037 ± 0.004	0.004 ± 0.001	0.005 ± 0.001	0.002 ± 0.001
Adrenals	0.036 ± 0.009	0.018 ± 0.005	0.003 ± 0.001	0.004 ± 0.003	0.0009 ± 0.0003
Stomach	0.722 ± 0.096	0.441 ± 0.055	0.058 ± 0.013	0.068 ± 0.010	0.012 ± 0.002
Small intestine	1.854 ± 0.462	1.390 ± 0.311	0.255 ± 0.153	0.204 ± 0.077	0.054 ± 0.012
Uterus	0.423 ± 0.161	0.196 ± 0.027	0.024 ± 0.012	0.029 ± 0.005	0.005 ± 0.001
Ovaries	0.070 ± 0.013	0.039 ± 0.008	0.005 ± 0.001	0.007 ± 0.002	0.0013 ± 0.0001
Blood	16.046 ± 2.363	7.076 ± 1.611	0.378 ± 0.062	0.542 ± 0.057	0.123 ± 0.019
Muscle	14.412 ± 2.549	10.222 ± 3.781	0.807 ± 0.138	0.891 ± 0.367	0.248 ± 0.056
Fat	1.473 ± 0.685	0.856 ± 0.158	0.154 ± 0.113	0.052 ± 0.019	0.013 ± 0.003
Bone	3.184 ± 0.658	1.784 ± 0.312	0.401 ± 0.240	0.372 ± 0.081	0.095 ± 0.018

Data are group mean of percentage injected activity (dose) per organ ± SD. Data are reported without applying decay correction. n = 6/group (3 males and 3 females); data for ovaries and uterus are n = 3/group.

to contrast-enhanced CT for detection of PE in renally insufficient patients. In terms of DVT, ^{64}Cu-FBP8 PET is not limited to the legs but could also be used to detect thrombi in iliac veins and calves, where ultrasonography has shown reduced efficacy (*34*). A concern in evaluation of DVT is delineating new thrombus from old clot in patients with a suspicion of recurrent DVT. Our findings in imaging animals with hyperacute versus days-old thrombi demonstrated that probe uptake was proportional to fibrin content and suggest that ^{64}Cu-FBP8 PET may be able to distinguish new from recurrent DVT. The ability of ^{64}Cu-FBP8 PET to detect differences in fibrin content may also inform interventional procedures. Younger thrombi are usually richer in fibrin and more likely to get lysed than mature, organized clots (*35*). Therefore, noninvasive assessment of clot composition may be useful for thrombus staging and to facilitate therapeutic choices (*9*). The ability of ^{64}Cu-FBP8 PET to detect both source thrombus and emboli in a single examination may also guide treatment decisions such as placement of a filter in the vena cava to prevent PE. Finally, ^{64}Cu-FBP8 PET offers the ability to monitor the effect of treatment. We recently showed that ^{64}Cu-FBP7, a close analog of ^{64}Cu-FBP8, could be used to monitor thrombolysis after embolic stroke in rats (*15*), and therefore we can anticipate comparable efficacy of ^{64}Cu-FBP8 to monitor treatment.

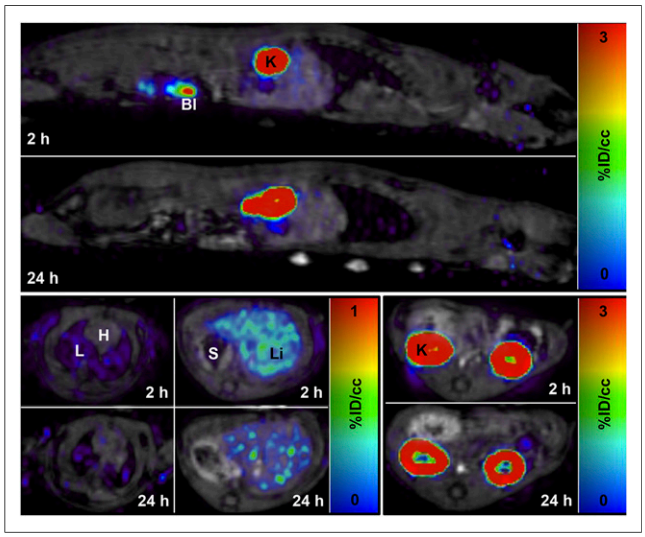

FIGURE 5. Whole-body ^{64}Cu-FBP8 PET/MR. Representative decay-corrected fused PET/MR images obtained from 60-min scans started 2 and 24 h after injection of ^{64}Cu-FBP8. Activity levels in renal cortices and urine are out of scale. n = 2. Bl = bladder; H = heart; K = kidney; L = lungs; Li = liver; S = stomach.

^{64}Cu is produced in a biomedical cyclotron by ^{64}Ni(p,n)^{64}Cu reaction, and although its availability is limited compared with other PET medical isotopes, its use has increased tremendously in recent years. A potential concern when using long-lived isotopes such as ^{64}Cu is the unfavorable dosimetry, which would limit the dose and result in poor image quality. However ^{64}Cu-FBP8 has high metabolic stability, extracellular distribution, and rapid renal elimination, resulting in effective doses that are similar to ^{18}F-FDG and ^{68}Ga-DOTATOC (*36,37*) and 40% lower than the hypoxia marker ^{64}Cu-diacetyl bis(N^4-methylthiosemicarbazone) (*38*). In the present study, the kidneys showed the highest absorbed dose, which may be further reduced in humans by increasing fluid intake and voiding more frequently after probe administration. On the other hand, the longer half-life of ^{64}Cu-FBP8 may be advantageous. In fact, it allows synthesis of the molecular probe in advance and even shipment-on-demand to sites far from a cyclotron, as well as delayed imaging when the activity in the systemic circulation is depleted but the activity in the thrombus would remain high, as we have shown (*16*). Finally, the simple and quantitative radiolabeling procedure

TABLE 2
Human Dosimetry Estimation

Organ	Adult male	Adult female
Kidneys	0.441	0.478
Liver	0.034	0.046
Bladder	0.146	0.198
Small intestine	0.008	0.009
Adrenals	0.007	0.009
Effective dose	0.021	0.027

Absorbed doses (α + β + photons) of main target organs and weighted effective doses are expressed as mSv/MBq.

for ^{64}Cu-FBP8 is also amenable to kit formulation, which would further lower the barrier to clinical adoption.

CONCLUSION

^{64}Cu-FBP8 PET is a feasible approach for whole-body thrombus detection, and the favorable dosimetry of ^{64}Cu-FBP8 in rats supports the translation in human trials.

DISCLOSURE

The costs of publication of this article were defrayed in part by the payment of page charges. Therefore, and solely to indicate this fact, this article is hereby marked "advertisement" in accordance with 18 USC section 1734. This work was supported by HL109448 from the National Heart, Lung, and Blood Institute. The small-animal PET/SPECT/CT system was funded by RR029495 from the National Center for Research Resources. Dr. Caravan has equity in Factor 1A, LLC, the company that holds the patent rights of the fibrin-binding peptide used in this study. No other potential conflict of interest relevant to this article was reported.

REFERENCES

1. Fedullo PF, Tapson VF. Clinical practice: the evaluation of suspected pulmonary embolism. *N Engl J Med.* 2003;349:1247–1256.
2. Stein PD, Fowler SE, Goodman LR, et al. Multidetector computed tomography for acute pulmonary embolism. *N Engl J Med.* 2006;354:2317–2327.
3. Ruiz Y, Caballero P, Caniego JL, et al. Prospective comparison of helical CT with angiography in pulmonary embolism: global and selective vascular territory analysis—Interobserver agreement. *Eur Radiol.* 2003;13:823–829.
4. PIOPED. Value of the ventilation/perfusion scan in acute pulmonary embolism: results of the prospective investigation of pulmonary embolism diagnosis (PIOPED). *JAMA.* 1990;263:2753–2759.
5. Anderson DR, Kahn SR, Rodger MA, et al. Computed tomographic pulmonary angiography vs ventilation-perfusion lung scanning in patients with suspected pulmonary embolism: a randomized controlled trial. *JAMA.* 2007;298:2743–2753.
6. Brotman DJ, Segal JB, Jani JT, Petty BG, Kickler TS. Limitations of D-dimer testing in unselected inpatients with suspected venous thromboembolism. *Am J Med.* 2003;114:276–282.
7. Heijboer H, Jongbloets LM, Buller HR, Lensing AW, ten Cate JW. Clinical utility of real-time compression ultrasonography for diagnostic management of patients with recurrent venous thrombosis. *Acta Radiol.* 1992;33:297–300.
8. Bounameaux H, Righini M, Perrier A. Venous thromboembolism: contemporary diagnostic and therapeutic aspects. *Vasa.* 2008;37:211–226.
9. Mehta BP, Nogueira RG. Should clot composition affect choice of endovascular therapy? *Neurology.* 2012;79:S63–S67.
10. Lindner JR. Molecular imaging of thrombus: technology in evolution. *Circulation.* 2012;125:3057–3059.
11. Ciesienski KL, Caravan P. Molecular MRI of thrombosis. *Curr Cardiovasc Imaging Rep.* 2010;4:77–84.
12. Uppal R, Catana C, Ay I, Benner T, Sorensen AG, Caravan P. Bimodal thrombus imaging: simultaneous PET/MR imaging with a fibrin-targeted dual PET/MR probe: feasibility study in rat model. *Radiology.* 2011;258:812–820.
13. Ciesienski KL, Yang Y, Ay I, et al. Fibrin-targeted PET probes for the detection of thrombi. *Mol Pharm.* 2013;10:1100–1110.
14. Boros E, Rybak-Akimova E, Holland JP, et al. Pycup: a bifunctional, cage-like ligand for ^{64}Cu radiolabeling. *Mol Pharm.* 2014;11:617–629.
15. Ay I, Blasi F, Rietz TA, et al. In vivo molecular imaging of thrombosis and thrombolysis using a fibrin-binding positron emission tomographic probe. *Circ Cardiovasc Imaging.* 2014;7:697–705.
16. Blasi F, Oliveira BL, Rietz TA, et al. Effect of chelate type and radioisotope on the imaging efficacy of 4 fibrin-specific PET probes. *J Nucl Med.* 2014;55:1157–1163.
17. Kolodziej AF, Nair SA, Graham P, et al. Fibrin specific peptides derived by phage display: characterization of peptides and conjugates for imaging. *Bioconjug Chem.* 2012;23:548–556.
18. Overoye-Chan K, Koerner S, Looby RJ, et al. EP-2104R: a fibrin-specific gadolinium-Based MRI contrast agent for detection of thrombus. *J Am Chem Soc.* 2008;130:6025–6039.
19. *Guide for the Care and Use of Laboratory Animals.* 8th ed. Washington, DC: National Academy Press; 2011.
20. Clozel JP, Holvoet P, Tschopp T. Experimental pulmonary embolus in the rat: a new in vivo model to test thrombolytic drugs. *J Cardiovasc Pharmacol.* 1988;12:520–525.
21. Kurz KD, Main BW, Sandusky GE. Rat model of arterial thrombosis induced by ferric chloride. *Thromb Res.* 1990;60:269–280.
22. Cai QY, Kim SH, Choi KS, et al. Colloidal gold nanoparticles as a blood-pool contrast agent for X-ray computed tomography in mice. *Invest Radiol.* 2007;42:797–806.
23. Loening AM, Gambhir SS. AMIDE: a free software tool for multimodality medical image analysis. *Mol Imaging.* 2003;2:131–137.
24. Lendrum AC, Fraser DS, Slidders W, Henderson R. Studies on the character and staining of fibrin. *J Clin Pathol.* 1962;15:401–413.
25. Saha P, Andia ME, Modarai B, et al. Magnetic resonance T1 relaxation time of venous thrombus is determined by iron processing and predicts susceptibility to lysis. *Circulation.* 2013;128:729–736.
26. Phinikaridou A, Andia M, Saha P, Modarai B, Smith A, Botnar R. In vivo magnetization transfer and diffusion-weighted magnetic resonance imaging detects thrombus composition in a mouse model of deep vein thrombosis. *Circ Cardiovasc Imaging.* 2013;6:433–440.
27. Andia ME, Saha P, Jenkins J, et al. Fibrin-targeted magnetic resonance imaging allows in vivo quantification of thrombus fibrin content and identifies thrombi amenable for thrombolysis. *Arterioscler Thromb Vasc Biol.* 2014;34:1193–1198.
28. Lee HB, Blaufox MD. Blood volume in the rat. *J Nucl Med.* 1985;26:72–76.
29. Brown RP, Delp MD, Lindstedt SL, Rhomberg LR, Beliles RP. Physiological parameter values for physiologically based pharmacokinetic models. *Toxicol Ind Health.* 1997;13:407–484.
30. Kirschner AS, Ice RD, Beierwaltes WH. Radiation dosimetry of ^{131}I-19-iodocholesterol. *J Nucl Med.* 1973;14:713–717.
31. Stabin MG, Sparks RB, Crowe E. OLINDA/EXM: the second-generation personal computer software for internal dose assessment in nuclear medicine. *J Nucl Med.* 2005;46:1023–1027.
32. Morris TA, Gerometta M, Yusen RD, et al. Detection of pulmonary emboli with ^{99m}Tc-labeled anti-D-dimer (DI-80B3)Fab' fragments (ThromboView). *Am J Respir Crit Care Med.* 2011;184:708–714.
33. Douketis JD, Ginsberg JS, Haley S, et al. Accuracy and safety of ^{99m}Tc-labeled anti-D-dimer (DI-80B3) Fab' fragments (ThromboView(R)) in the diagnosis of deep vein thrombosis: a phase II study. *Thromb Res.* 2012;130:381–389.
34. Zierler BK. Ultrasonography and diagnosis of venous thromboembolism. *Circulation.* 2004;109:I9–I14.
35. Brommer EJ, Potter van Loon BJ, Rijken DC, van Bockel JH. Composition and susceptibility to thrombolysis of pathological human arterial thrombi. *Ann N Y Acad Sci.* 1992;667:283–285.
36. Hays MT, Watson EE, Thomas SR, Stabin M. MIRD dose estimate report no. 19: radiation absorbed dose estimates from ^{18}F-FDG. *J Nucl Med.* 2002;43:210–214.
37. Sandström M, Velikyan I, Garske-Roman U, et al. Comparative biodistribution and radiation dosimetry of ^{68}Ga-DOTATOC and ^{68}Ga-DOTATATE in patients with neuroendocrine tumors. *J Nucl Med.* 2013;54:1755–1759.
38. Laforest R, Dehdashti F, Lewis JS, Schwarz SW. Dosimetry of 60/61/62/^{64}Cu-ATSM: a hypoxia imaging agent for PET. *Eur J Nucl Med Mol Imaging.* 2005;32:764–770.